THE JOURNAL OF
PHYSICAL CHEMISTRY C

Effect of Sn Doping on Surface States of Bi_2Se_3 Thin Films

Gregory M. Stephen,* Ivan Naumov, Siddharth Tyagi, Owen A. Vail, Jennifer E. DeMell, Michael Dreyer, Robert E. Butera, Aubrey T. Hanbicki, Patrick J. Taylor, Isaak Mayergoyz, Pratibha Dev, and Adam L. Friedman*

Cite This: https://dx.doi.org/10.1021/acs.jpcc.0c07176

ABSTRACT: Bi_2Se_3, widely studied as a topological insulator, has great potential for applications in low-power electronics and quantum computing. Intrinsic doping, however, presents a persistent challenge, leading to predominantly bulk conduction. In this work, we use substitutional Sn dopants to control the Fermi level in Bi_2Se_3 films. Scanning tunneling microscopy (STM) shows a shift in the local density of states toward the Dirac point as more Sn is incorporated. Density functional theory calculations elucidate the STM results, showing that Sn adds metallic states near the Fermi level that are localized to the defect sites while leaving the Dirac cone undisturbed. Electronic transport measurements demonstrate that the Sn defects increase the separation between bulk and surface states, though bulk conduction remains a dominant component.

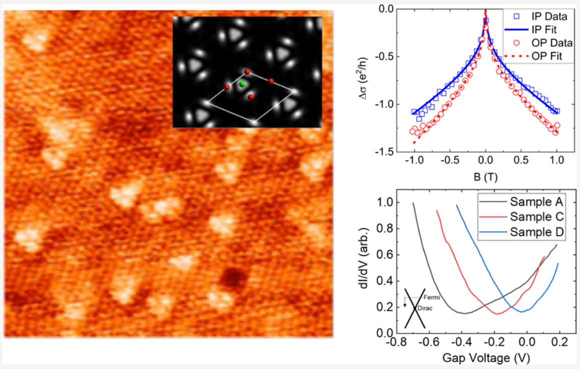

INTRODUCTION

In a post-CMOS paradigm, extending the fast computational gains envisioned by Moore's law for high-performance computing requires novel devices utilizing alternate state variables.[1,2] Spintronic devices, such as various MRAM designs and spinFETs, utilize the spin degree of freedom, which can allow for lower power dissipation, higher device density, and nonvolatility unlike conventional Si and CMOS-based electronics.[3−6] Such devices require efficient spin-to-charge conversion, long spin-diffusion lengths, and controllable spin relaxation.[7,8] Control of the spin relaxation can be achieved through spin−orbit coupling (SOC), although it is detrimental to long spin diffusion lengths as it introduces additional scattering.[9,10] Topological insulators (TIs) can be used to circumvent this roadblock via topologically protected surface states.[11,12] TIs are characterized by a linear dispersion in their surface bands, referred to as a Dirac cone, at the center of which the conductance and valence bands meet at a single "Dirac" point where the conductivity is expected to be minimized.[13−15] The surface states associated with these bands are accompanied by spin-momentum locking and are thus protected from backscattering by the band topology. Finally, TIs have significant SOC which should enable control of the spin relaxation. Unfortunately, TIs are often intrinsically doped such that the non-topological bulk conduction overwhelms that of the surface, resulting in metallic behavior.[15,16]

Among the TIs, Bi_2Se_3 is widely studied due to the relative ease of thin-film growth and the simplicity of the band structure, with one Dirac cone at the gamma point and a large band gap (~0.3 eV).[13] However, because of Se vacancies, samples are heavily n-doped leading to a significant contribution from the bulk. In order to effectively utilize Bi_2Se_3, the bulk contribution must be minimized. Gating has been used to modulate the conductivity, but the bulk contribution continues to dominate in these samples.[17,18] Elemental doping is a promising pathway to minimize the bulk conductivity by changing the intrinsic carrier density. Mg, Mn, and Ca have been used as p-type dopants for Bi_2Se_3, which is naturally n-type due to Se vacancies, though the resulting insulating behavior remains weak.[19−21] Cu and Pd doping were reported to introduce a superconducting transition.[22] Alloying Bi_2Se_3 and Bi_2Te_3 has shown mixed results, where the alloyed films are often still heavily doped.[16,23,24] Sn is a promising p-type dopant which is predicted to create resonant levels near the valence bands,[25] minimizing the interference with the electronic gap.

In this work, we study 400 nm thick Sn-doped Bi_2Se_3 grown via molecular beam epitaxy (MBE) with doping levels varying up to 5%. Scanning tunneling microscopy (STM) images likely show Sn dopants at the surface, closely matching with our first-principles calculations. Local differential conductance (dI/dV) curves show the Dirac point indeed moving toward the Fermi

Received: August 5, 2020
Revised: October 13, 2020

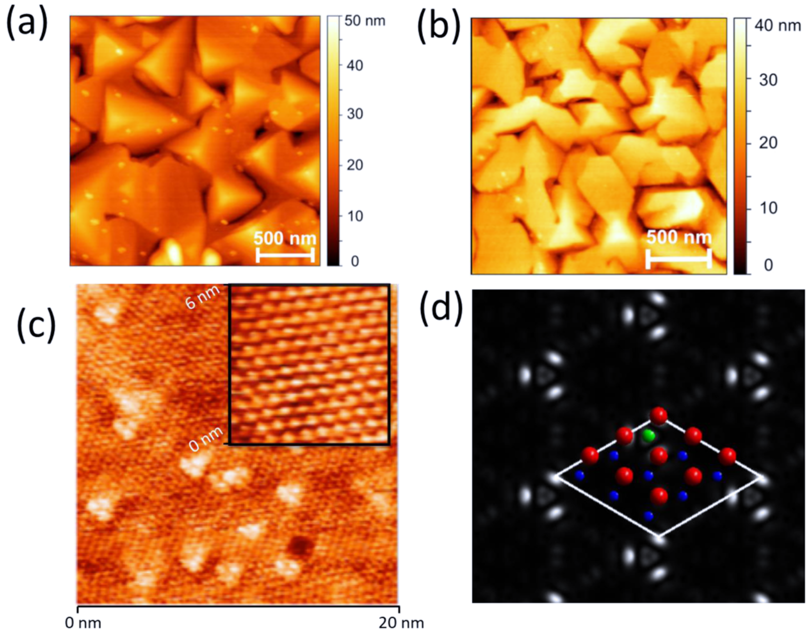

Figure 1. (a,b) AFM scans of (a) sample A with intrinsic doping and (b) sample D with 4.9% Sn doping. (c) STM images at room temperature for samples A (inset) and D. The bright spots correspond to the Sn defects and adjacent Se sites, as demonstrated by (d) the theoretical STM surface reconstruction. The Sn site is shown in green with Se in red.

level with increasing Sn doping. Surprisingly, Hall measurements show a persistently high, 10^{19} cm^{-3}, n-type carrier density regardless of Sn doping level, likely resulting from an increase in Se vacancies in the bulk. Magnetoresistance (MR) shows a strong quadratic background that decreases with doping, accompanied by weak antilocalization (WAL) that becomes stronger at higher doping, which could indicate a separation of bulk and surface states. These results indicate that the Sn dopants have the desired effect of moving the Dirac point toward the Fermi level, while increasing the bulk carrier density. At sufficiently high doping levels, Sn adds an additional conduction channel through the Sn defects.

■ METHODS

Sample Growth. The growth of Sn-doped Bi_2Se_3 by MBE was accomplished using high-purity elemental sources of Bi, Sn, and Se. To facilitate the characterization of Sn-doped film properties, the epitaxial layers were grown on semi-insulating (001) GaAs substrates. Before initiating MBE growth, the GaAs substrates were thermally cleaned in ultra-high vacuum (UHV) and exposed to a flux of Se vapor such that a termination layer of Ga_2Se_3 exhibiting a (2 × 1) surface reconstruction is obtained at a growth temperature of 260 °C. MBE was then initiated by exposing the surface to a combined flux of Bi, Se, and Sn. The flux ratio of Se-to-Bi was about 10, and the range of Sn doping was obtained by varying the Sn flux. Films are denoted as A, B, C, and D where the corresponding Sn concentrations as a percentage of the Bi are (A = 0%, B = 0.73%, C = 2.16%, D = 4.9%), measured as the ratio of Sn-flux to Bi-flux during growth. Growth proceeded with a *c*-axis orientation, and visually, all obtained films were remarkably specular. As shown in Figure 1a,b, the obtained films exhibited a domain size of roughly 500 nm, with root mean square roughness on the order of 1−4 nm. Atomic force microscopy (AFM) images and X-ray diffractograms of all films are given in Supporting Information Figures S6 and S7.

Measurement Details. Atomic resolution STM micrographs and d*I*/d*V* curves are measured in an Omicron STM at room temperature in UHV, with voltage applied to the sample and the tip at virtual ground.[26,27] To prepare pristine surfaces for STM, a metallic post is glued to the sample surface with non-conducting epoxy and the post is mechanically removed in the chamber under UHV, resulting in a freshly cleaved surface. Data is taken using standard lock-in techniques[28] and with electrochemically etched W tips that were e-beam annealed in vacuum. AFM scans are taken in a Bruker Dimension Icon AFM in ambient conditions. To probe the macroscopic transport behavior, MR and Hall effect measurements are carried out in a closed-cycle variable-temperature (3−300 K) cryostat suspended between the poles of a 1 T electromagnet and mounted on a variable angle platform. Hall bar samples (10 μm × 20 μm) are defined using an Ar plasma etch, with e-beam deposited Ti/Au contact pads.

Computations. Electronic structure calculations were performed using the projector-augmented wave method[29] as implemented in the VASP package.[30] Fully relativistic calculations were carried out to include SOC, which plays a significant role in the electronic structure of Bi_2Se_3. Exchange−correlation effects were taken into account within the Perdew−Burke−Ernzerhof (PBE) approximation.[31] The kinetic energy cut-off was set to 400 eV. We chose a 25 Å thick vacuum gap to prevent interaction between the replica films. Bi_2Se_3 thin films were formed by stacking *n* quintuple layers (QLs) of Bi_2Se_3 ($n = 2, 3, 4$) along the trigonal axis. Such a termination is most stable because it breaks only weak van der Waals bonds. In order to understand how doping with Sn affects the electronic structure properties of Bi_2Se_3, we added Sn atoms in the Bi-subsurface layer substitutionally, while the topmost surface layer was occupied by Se atoms. The concentration of the Sn atoms within a layer was controlled by setting different in-plane (IP) lattice parameters of the supercell. We studied the effect of Sn-dopants in 2 × 2 × 3 QL, 2 × 2 × 4 QL, 2 × 2 × 6 QL, 3 × 3 × 4 QL, and 4 × 4 × 2 QL, reserving $n = 2$ QL

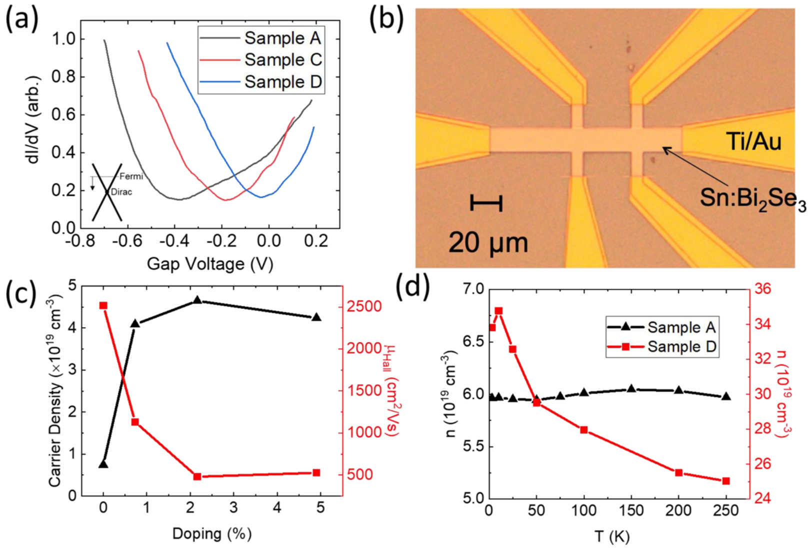

Figure 2. (a) Local dI/dV curves at room temperature for samples A, C, and D. Each curve is an average of 20 scans. The minimum corresponds to the charge neutrality (Dirac) point. As Sn-doping increases, the Fermi energy moves relative to the Dirac point, as shown in the inset. (b) Hall bar layout. (c) Carrier density (black) and Hall mobility (red) as a function of Sn doping at 3 K. The carrier density increases with Sn doping, in contrast to the dI/dV results. (d) Temperature dependence of carrier density n for samples A and D. The carrier density for sample A stays relatively constant while the density for sample D decreases by 25%.

for larger supercells due to the computational cost. During structural relaxations, the IP lattice parameter of the films was kept to the bulk value and the atoms were allowed to move to relax both forces and out-of-plane (OP) stresses. To simulate STM images, we used the so-called Tersoff−Hamann's model, in which the unknown electronic structure of the tip is assumed to be an atomic s-wave-function. Within this model, the tunneling current is defined by integrating over energy the product of two quantities: the local density of states (LDOS) of the tip and the LDOS of the sample at the position of the tip apex atom.

■ RESULTS AND DISCUSSION

AFM micrographs of samples A and D are shown in Figure 1a,b respectively. The intrinsic film (sample A) shows the expected triangular crystallites merged into a continuous film as observed in the literature.[32] Sample D has a similar microstructure, but with hexagonal islands. The absolute roughness, or corrugation, between the islands is similar between the two films. Figure 1c shows atomic resolution STM surface scans at room temperature in UHV for sample D, with the sample A in the inset at a tunneling current of 300 pA and bias voltage of 200 mV. The Sn dopants are likely visible as bright triangular spots in the sample D image, features which are absent in sample A. Similar triangular features are attributed to anti-site defects in other studies[26] and charged Se vacancies. Nonetheless, the absence of such features in sample A and the difference in expected sizes of these features and what we observe suggest they are in fact Sn dopants.

Figure 1d shows the calculated STM surface scan with periodic Sn dopants (calculation details are given below). The green sphere corresponds to the location of the Sn dopant, blue spheres are the Bi-atoms, and the red spheres represent the surface Se layer. The triangular bright/dark spots are similar to the bright spots observed in sample D STM scan, indicating that the bright spots are likely from the Sn dopants, further discussed in depth below.

Local dI/dV curves measured via STM at room temperature are shown in Figure 2a. The LDOS is proportional to dI/dV, providing a direct measurement of the local electronic structure. Because the LDOS is proportional to the differential conductance, dI/dV, STM provides a direct measurement of the local electronic structure. As doping density increases, the dI/dV minimum (Dirac point) moves toward zero (Fermi energy), indicating that the Fermi energy is moving toward the Dirac point (Figure 2a-inset), implying a reduction in carrier concentration as expected.[27,33] The carrier density and Hall mobility, found by measuring devices patterned into Hall bars as shown in Figure 2b, are plotted versus doping percentage in Figure 2c. The bulk carrier density (Figure 2c black triangles, left axis) increases quickly with Sn doping, staying relatively constant between samples B, C, and D. The increased carrier density correlates with a 5-fold decrease in Hall mobility (Figure 2c red squares, right axis). This is in contrast to the dI/dV scans where the movement of the Fermi level toward the Dirac point suggests a decreasing carrier density. The increase in bulk carrier density likely results from an increase in Se vacancies with the addition of Sn. The apparent discrepancy can be explained by the local and surface-sensitive nature of the STM probe. At the surface, the electronic structure is dominated by the Dirac cone, so additional carriers will shift the Fermi level such that the Dirac point moves towards zero, as seen in the dI/dV scans. However, the Hall measurement averages over the entire film, which is 400 nm thick. The localized nature of the Sn means that the overall conduction is still governed by the bulk bands. Figure 2d shows the temperature dependence of the carrier concentration for samples A (black triangles, left axis) and D (red squares, right axis). As a function of temperature, the carrier concentration is relatively constant at 6×10^{19} cm^{-3} for the intrinsic sample. For sample D, at low temperature, the carrier concentration is much higher at 3.4×10^{20} cm^{-3} and there is a 30% decrease between 10 and 300 K. The resistivity increases from 1.6×10^{-5} to 5.4×10^{-5} Ωm as the carrier concentration

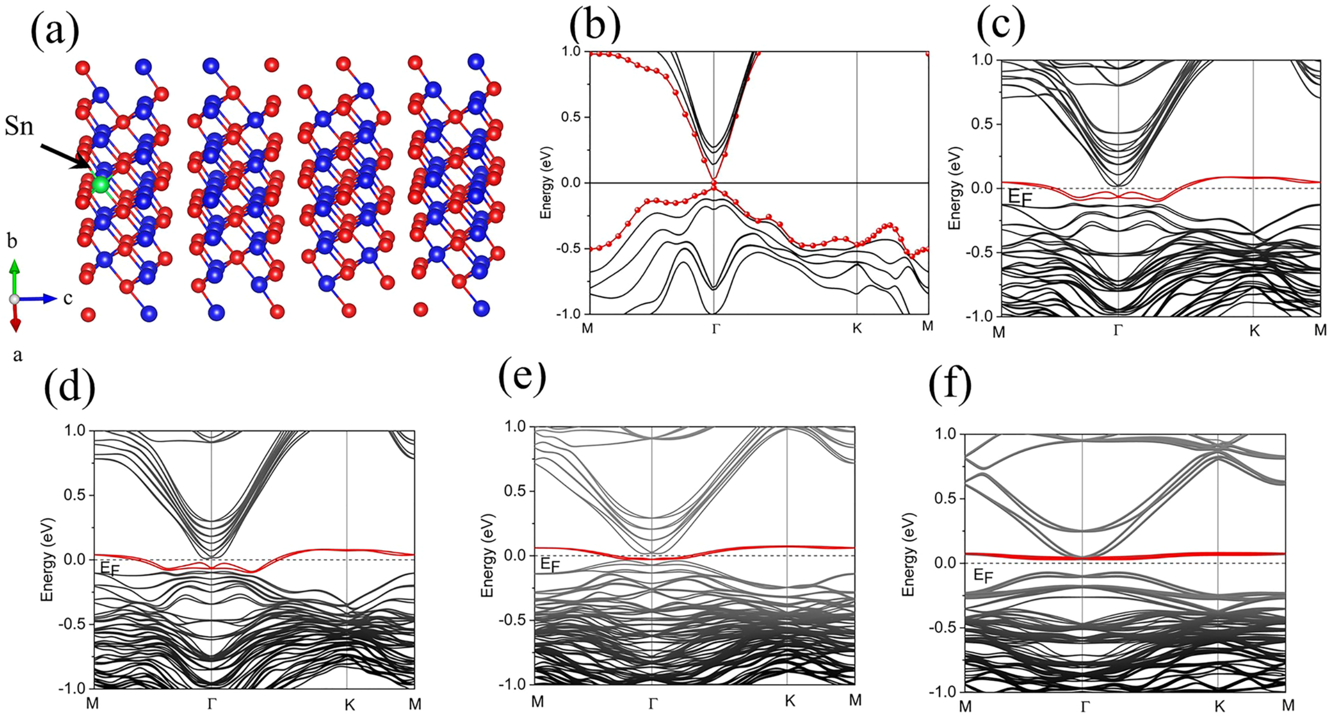

Figure 3. (a) View of the supercell 3 × 3 × 4 QL containing 4 QLs and 180 atoms: 71 Bi atoms (shown in red), one Sn atom (shown in green), and 108 Se atoms (shown in blue). (b−f) Band structures of Bi_2Se_3 thin films: (b) a 4 QL-thick pure Bi_2Se_3 slab. The red lines indicate the topological surface states. The Dirac point is where the conduction and valence bands meet at $E = 0$ eV. (c) 2 × 2 × 4 QL with a thickness of four QLs and stoichiometry of $Bi_{31}Sn_1Se_{48}$, (d) 2 × 2 × 6 QL ($Bi_{47}Sn_1Se_{72}$) (e) 3 × 3 × 4 QL ($Bi_{71}Sn_1Se_{108}$), and (f) 4 × 4 × 2 QL ($Bi_{63}Sn_1Se_{96}$), roughly corresponding to the doping levels in the samples measured in this study. The red lines indicate the "impurity" states associated with the Sn atoms and localized near the surface.

decreases in this temperature range (see Supporting Information Figure S3).

In order to understand the origin of the STM images and film behavior, we investigated the electronic structure of Bi_2Se_3 thin films using density functional theory (DFT). Bi_2Se_3 thin films were formed by stacking n QLs of Bi_2Se_3 ($n = 2, 3, 4$) along the trigonal axis. The Sn-dopant is more likely to substitute a Bi-atom in the lattice rather than a Se-atom as: (i) the ionic radius of Sn^{4+} (83 pm) is considerably closer to that of Bi^{5+} (90 pm) than to the radius of Se^{4+} (64 pm), and (ii) Pauling electronegativity of Sn (1.96) is closer to that of Bi (2.02) than that of Se (2.55). Our direct calculations support this intuition. We compared the energies of two different processes: (i) Sn goes in the Bi site in the subsurface layer, with the replaced Bi going into vacuum as a free atom, and (ii) Sn substitutes a Se-atom in the top surface layer, with the replaced Se going into vacuum as a free atom. We found that the first process associated with Bi substitution is energetically more favorable than the second process by ∼3.3 eV. Hence, the Sn atoms were added in the Bi-subsurface layer substitutionally (Figure 3a), while the topmost surface layer was occupied by Se atoms, with the Se atoms above Sn arranged at the corners of a triangle. In the relaxed structure, these Se atoms in the top surface layer, which sit just above the Sn atoms, move inward with the Se−Se distance decreasing by 3%. Using this structural model, we can simulate STM images, and in our calculations, the STM images are very similar for all the supercell sizes studied here. The simulation presented in Figure 1d is for the case of 3 × 3 × 4 QL, and shows a periodic set of triangular bright spots. This type of defect pattern has been observed for other types of substitutions such as Bi antisites and Cu dopants.[33] The center of the bright triangles coincides with the Se atoms that sit just above the Sn dopants. This is because Sn atoms introduce s- and p_z-derived impurity states that hybridize with the Se π^* states. As a result, the main contribution to the tunneling current stems from the Se atoms that are closest to the impurity and form equilateral triangles. Our simulated STM images show good agreement with the experimentally observed triangles, implying that Sn indeed substitutes Bi as expected. STM simulations with Sn substituting for Se as well as Se vacancies are shown in Supporting Information Figure S4. Both neutral and Se^{2+} vacancies are calculated, with the charged vacancies showing a triangular feature. However, the change in DOS produced by the charged vacancy is significantly smaller than what is observed in our samples which extends across several atoms. Furthermore, no such features are observed in the undoped-sample, further validating Sn-Bi substitution.

Figure 3b−f shows the band structure of pure and doped Bi_2Se_3 thin films. For the intrinsic material (Figure 3b), 4 QL was used. Figure 3c−f corresponds to a Sn-dopant in 3 QL through 6 QL respectively. From Figure 3b, one can see that a thickness of 4 QL is enough to reproduce the topological Dirac cone,[13] though the crossover to the 3D behavior is known to occur at 6 QL.[34] When the Sn dopants are introduced, two new weakly dispersive impurity bands appear within the "bulk" energy gap over the entire Brillouin zone (shown in red in Figure 3c−f). They are derived from the s- and p_z-orbitals of Sn and energetically overlap with the topological surface bands. By comparing the band structure for 2 × 2 × 3 QL shown in Figure 3c with that for 2 × 2 × 4 QL in Figure 3d, one can see that for the thicker film, but with the same dopant

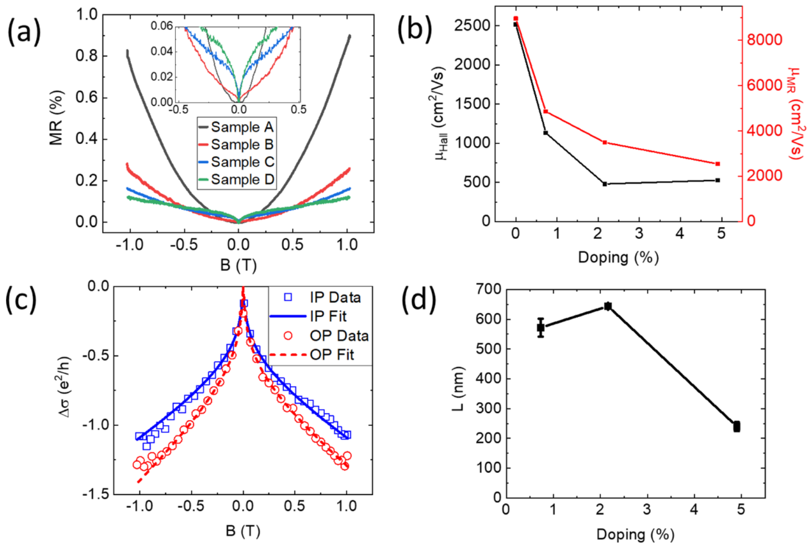

Figure 4. (a) MR at $T = 3$ K for all doping levels. The quadratic contribution decreasing with increasing Sn doping, while the WAL contribution increases. There is no WAL contribution for sample A. (b) MR mobility and Hall mobility versus doping at $T = 3$ K. The similar trend indicates that the background comes from geometric magnetoresistance. (c) WAL fitting for sample D with OP (red) and IP (blue) magnetic fields. The OP data is fit with the HLN model to get (d) the phase coherence length as a function of doping. The IP field data is fit to the Tkachov−Hankiewicz model, yielding an effective skin depth of 90 nm for sample D.

concentration, the character of the impurity bands does not change appreciably. Due to computational cost, the number of QLs in the supercell is limited, thus the Dirac cone is not fully recreated as it would be for thicker films (see Supporting Information Figure S5).[27] A pure bulk calculation without a vacuum gap is given in Supporting Information Figure S6, which shows that the Sn defect band exists throughout the entire film. On the other hand, as one decreases the dopant concentration (compare Figure 3d−f), the impurity bands become progressively flatter. The impurity bands do not show any tendency to make the connection between the "bulk" conduction and valence bands, as one would expect keeping in mind the topological nature of Bi_2Se_3. Furthermore, as the bands under discussion cross the Fermi level, new 2D Fermi surfaces may appear, thereby increasing the DOS at the Fermi level. In this context, the Sn dopant makes the bulk conduction more metallic.

With the STM images demonstrating reduced metallicity locally with Sn doping and Hall measurements showing an increase in conductivity, we use magnetotransport measurements to further explore the macroscopic electronic behavior. Figure 4a shows the MR at 3 K for the measured samples. The measured MR consists of a quadratic component and a low-field cusp. The quadratic component is attributed to geometric MR where MR = $\mu_{MR}{}^2B^2$,[35] and the cusp corresponds to WAL. No WAL is observed in the intrinsic Bi_2Se_3, but as doping increases, the WAL cusp emerges and becomes stronger while the quadratic background decreases. This suggests the contribution from the topological states gets stronger with Sn-doping. Figure 4b compares the MR mobility (μ_{MR}) and Hall mobility (μ_{Hall}) versus doping. Qualitatively, the two values exhibit similar trends as a function of doping level, demonstrating that the decrease in quadratic background mostly stems from Sn decreasing the carrier mobility. The WAL that emerges with doping is fit to the Hikami−Larkin−Nagaoka (HLN) model to extract the phase coherence length.[36,37] The conductivity is described by

$$\frac{\Delta\sigma_{xx,\perp}}{\sigma_0} = \frac{\alpha e^2}{2\pi h}\left[\psi\left(\frac{B_\perp}{B} + \frac{1}{2}\right) - \ln\left(\frac{B_\perp}{B}\right)\right] \tag{1a}$$

$$B_\perp = \frac{\hbar}{2eL^2} \tag{1b}$$

The coefficient α is 1/2 for each conduction channel. The resulting coherence length L is plotted versus doping in Figure 4d. Additionally, the fit yields a value of the coefficient $\alpha = 0.82$ and 0.87 for B and C samples, respectively, while sample D yields $\alpha = 1.4$. Because the thickness of these films is 400 nm, the top and bottom surfaces should be effectively decoupled giving two conduction channels, yielding $\alpha \approx 1$,[38,39] as is seen in samples B and C. In sample D, the Sn-dopants are at a high enough density to produce an additional conduction channel, yielding $\alpha \approx 1.5$. The increase in α is accompanied by a decrease in L, suggesting that the Sn conduction channel has considerably weaker phase coherence than the surface states.

An increase in WAL is often explained by an increase in SOC. However, as Sn is lighter than Bi, this substitution should lead to a decrease in average SOC strength. Additionally, the observed decrease in mobility, Figure 4b, suggests that the localization length is decreasing, which also would have a mitigating effect. The increased WAL, therefore, most likely results from an increased surface state contribution.

In addition to measuring the WAL with out-of-plane (OP) magnetic fields, in-plane (IP) fields can be used to investigate the extent and quality of the surface states.[23,40] MR versus field for both field directions is given in the Supporting Information Figure S7. Only samples B and D showed IP MR. The IP magnetoconductance can be fit to the Tkachov−Hankiewicz model to extract an effective skin depth of the surface states. In this model, for an IP field, the magnetoconductance is described by[41]

$$\frac{\Delta\sigma_{xx,\parallel}}{\sigma_0} = -\frac{e^2}{2\pi h}\ln\left(1 + \frac{B^2}{B_\parallel{}^2}\right) \tag{2a}$$

$$B_{\parallel} = \frac{2L}{\lambda}B_{\perp} = \frac{\hbar}{\lambda eL} \tag{2b}$$

where λ is the effective skin depth. The WAL cusp in sample B is nearly independent of the field angle, indicating a mostly 3D origin (see Supporting Information) and therefore mostly unrelated to the 2D surface states. However, the angle dependence in Sample D is well explained by the Tkachov–Hankiewicz model (Figure 4c), which gives an effective skin depth of 90 nm. This is considerably thinner than the 400 nm sample thickness but much larger than the expected 4 nm skin depth.[42] The absolute film roughness, which is on the order of 30 nm, will smear the surface states due to depinning and increases in Fermi velocity.[43]

CONCLUSIONS

These results demonstrate that Sn dopants in Bi_2Se_3 introduce localized metallic states and induce a shift in the Fermi level toward the Dirac point. The shift in the Fermi level correlates with an increase in WAL, indicating an increased surface state contribution. The macroscopic electronic transport is governed by bulk conduction, due to the additional carriers added by the Se vacancies and the thickness of our film. Overall, we find that Sn doping is a promising method for enhancing the surface states in Bi_2Se_3 as compared to the bulk. Further material optimization, such as incorporating Sn into smoother films as well as better control over Se vacancies, could lead to better control of the Dirac point.

ASSOCIATED CONTENT

Supporting Information

The Supporting Information is available free of charge at https://pubs.acs.org/doi/10.1021/acs.jpcc.0c07176.

> Additional resistivity measurements, versus both field and temperature, further DFT calculations, AFM scans of all samples, and X-ray diffractograms (PDF)

AUTHOR INFORMATION

Corresponding Authors

Gregory M. Stephen − *Laboratory for Physical Sciences, College Park, Maryland 20740, United States;* Email: gstephen@lps.umd.edu

Adam L. Friedman − *Laboratory for Physical Sciences, College Park, Maryland 20740, United States;* orcid.org/0000-0003-0597-5432; Email: afriedman@lps.umd.edu

Authors

Ivan Naumov − *Department of Physics and Astronomy, Howard University, Washington, D.C. 20059, United States*

Siddharth Tyagi − *Department of Electrical and Computer Engineering, University of Maryland, College Park, Maryland 20742, United States*

Owen A. Vail − *Army Research Laboratory, Adelphi, Maryland 20783, United States*

Jennifer E. DeMell − *Laboratory for Physical Sciences, College Park, Maryland 20740, United States*

Michael Dreyer − *Department of Physics, University of Maryland, College Park, Maryland 20740, United States*

Robert E. Butera − *Laboratory for Physical Sciences, College Park, Maryland 20740, United States;* orcid.org/0000-0003-2063-2446

Aubrey T. Hanbicki − *Laboratory for Physical Sciences, College Park, Maryland 20740, United States;* orcid.org/0000-0001-8200-0378

Patrick J. Taylor − *Army Research Laboratory, Adelphi, Maryland 20783, United States*

Isaak Mayergoyz − *Department of Electrical and Computer Engineering, University of Maryland, College Park, Maryland 20742, United States*

Pratibha Dev − *Department of Physics and Astronomy, Howard University, Washington, D.C. 20059, United States*

Complete contact information is available at: https://pubs.acs.org/10.1021/acs.jpcc.0c07176

Notes

The authors declare no competing financial interest.

ACKNOWLEDGMENTS

The authors gratefully acknowledge critical assistance from LPS support staff including G. Latini, J. Wood, R. Brun, P. Davis, and D. Crouse. The authors gratefully acknowledge support from the Applied Research for the Advancement of S&T Priorities program of the Office of the Secretary of Defense. P.D. and I.N. acknowledge support from W. M. Keck Research Foundation grant and National Science Foundation grant no. DMR-1752840. P.D. and I.N. also acknowledge the computational support provided by the Extreme Science and Engineering Discovery Environment (XSEDE) under project no. PHY180014, which is supported by National Science Foundation grant no. ACI-1548562.

REFERENCES

(1) Mack, C. A. Fifty Years of Moore's Law. *IEEE Trans. Semicond. Manuf.* **2011**, *24*, 202−207.

(2) Wolf, S. A. Spintronics: A Spin-Based Electronics Vision for the Future. *Science* **2001**, *294*, 1488−1495.

(3) Thompson, S. E.; Parthasarathy, S. Moore's Law: The Future of Si Microelectronics. *Mater. Today* **2006**, *9*, 20−25.

(4) Behin-Aein, B.; Datta, D.; Salahuddin, S.; Datta, S. Proposal for an All-Spin Logic Device with Built-in Memory. *Nat. Nanotechnol.* **2010**, *5*, 266−270.

(5) Wang, K. L.; Alzate, J. G.; Khalili Amiri, P. Low-Power Non-Volatile Spintronic Memory: STT-RAM and Beyond. *J. Phys. D: Appl. Phys.* **2013**, *46*, 074003.

(6) Žutić, I.; Fabian, J.; Das Sarma, S. Spintronics: Fundamentals and Applications. *Rev. Mod. Phys.* **2004**, *76*, 323−410.

(7) Ghiasi, T. S.; Kaverzin, A. A.; Blah, P. J.; van Wees, B. J. Charge-to-Spin Conversion by the Rashba-Edelstein Effect in Two-Dimensional van der Waals Heterostructures up to Room Temperature. *Nano Lett.* **2019**, *19*, 5959−5966.

(8) Safeer, C. K.; Ontoso, N.; Ingla-Aynés, J.; Herling, F.; Pham, V. T.; Kurzmann, A.; Ensslin, K.; Chuvilin, A.; Robredo, I.; Vergniory, M. G.; et al. Large Multidirectional Spin-to-Charge Conversion in Low-Symmetry Semimetal $MoTe_2$ at Room Temperature. *Nano Lett.* **2019**, *19*, 8758−8766.

(9) Friedman, A. L.; McCreary, K. M.; Robinson, J. T.; van 't Erve, O. M. J.; Jonker, B. T. Spin Relaxation and Proximity Effect in WS_2/Graphene/Fluorographene Non-Local Spin Valves. *Carbon* **2018**, *131*, 18−25.

(10) Huertas-Hernando, D.; Guinea, F.; Brataas, A. Spin-Orbit-Mediated Spin Relaxation in Graphene. *Phys. Rev. Lett.* **2009**, *103*, 146801.

(11) Liu, L.; Richardella, A.; Garate, I.; Zhu, Y.; Samarth, N.; Chen, C. T. Spin-Polarized Tunneling Study of Spin-Momentum Locking in Topological Insulators. *Phys. Rev. B: Condens. Matter Mater. Phys.* **2015**, *91*, 235437.

(12) Li, C. H.; van't Erve, O. M. J.; Robinson, J. T.; Liu, Y.; Li, L.; Jonker, B. T. Electrical Detection of Charge-Current-Induced Spin Polarization Due to Spin-Momentum Locking in Bi_2Se_3. *Nat. Nanotechnol.* **2014**, *9*, 218−224.

(13) Zhang, H.; Liu, C.-X.; Qi, X.-L.; Dai, X.; Fang, Z.; Zhang, S.-C. Topological Insulators in Bi_2Se_3, Bi_2Te_3 and Sb_2Te_3 with a Single Dirac Cone on the Surface. *Nat. Phys.* **2009**, *5*, 438−442.

(14) Bansil, A.; Lin, H.; Das, T. Colloquium: Topological Band Theory. *Rev. Mod. Phys.* **2016**, *88*, 021004.

(15) Jafarpisheh, S.; Ju, A.; Janßen, K.; Taniguchi, T.; Watanabe, K.; Stampfer, C.; Beschoten, B. Reducing the Impact of Bulk Doping on Transport Properties of Bi-Based 3D Topological Insulators. *Phys. Status Solidi B* **2020**, 200021.

(16) Ren, Z.; Taskin, A. A.; Sasaki, S.; Segawa, K.; Ando, Y. Large Bulk Resistivity and Surface Quantum Oscillations in the Topological Insulator Bi_2Te_2Se. *Phys. Rev. B: Condens. Matter Mater. Phys.* **2010**, *82*, 241306.

(17) Son, J.; Banerjee, K.; Brahlek, M.; Koirala, N.; Lee, S.-K.; Ahn, J.-H.; Oh, S.; Yang, H. Conductance Modulation in Topological Insulator Bi_2Se_3 Thin Films with Ionic Liquid Gating. *Appl. Phys. Lett.* **2013**, *103*, 213114.

(18) Kong, D.; Dang, W.; Cha, J. J.; Li, H.; Meister, S.; Peng, H.; Liu, Z.; Cui, Y. Few-Layer Nanoplates of Bi_2Se_3 and Bi_2Te_3 with Highly Tunable Chemical Potential. *Nano Lett.* **2010**, *10*, 2245−2250.

(19) Butch, N. P.; Kirshenbaum, K.; Syers, P.; Sushkov, A. B.; Jenkins, G. S.; Drew, H. D.; Paglione, J. Strong Surface Scattering in Ultrahigh-Mobility Bi_2Se_3 Topological Insulator Crystals. *Phys. Rev. B: Condens. Matter Mater. Phys.* **2010**, *81*, 241301.

(20) Choi, Y. H.; Jo, N. H.; Lee, K. J.; Lee, H. W.; Jo, Y. H.; Kajino, J.; Takabatake, T.; Ko, K.-T.; Park, J.-H.; Jung, M. H. Simple Tuning of Carrier Type in Topological Insulator Bi_2Se_3 by Mn Doping. *Appl. Phys. Lett.* **2012**, *101*, 152103.

(21) Analytis, J. G.; Chu, J.-H.; Chen, Y.; Corredor, F.; McDonald, R. D.; Shen, Z. X.; Fisher, I. R. Bulk Fermi Surface Coexistence with Dirac Surface State in Bi_2Se_3: A Comparison of Photoemission. *Phys. Rev. B: Condens. Matter Mater. Phys.* **2010**, *81*, 205407.

(22) Hor, Y. S.; Checkelsky, J. G.; Qu, D.; Ong, N. P.; Cava, R. J. Superconductivity and Non-Metallicity Induced by Doping the Topological Insulators Bi_2Se_3 and Bi_2Te_3. *J. Phys. Chem. Solids* **2011**, *72*, 572−576.

(23) Stephen, G. M.; Vail, O. A.; Lu, J.; Beck, W. A.; Taylor, P. J.; Friedman, A. L. Weak Antilocalization and Anisotropic Magnetoresistance as a Probe of Surface States in Topological $Bi_2Te_xSe_{3-x}$ Thin Films. *Sci. Rep.* **2020**, *10*, 4845.

(24) Kapustin, A. A.; Stolyarov, V. S.; Bozhko, S. I.; Borisenko, D. N.; Kolesnikov, N. N. Surface origin of quasi-2D Shubnikov-de Haas oscillations in Bi_2Te_2Se. *J. Exp. Theor. Phys.* **2015**, *121*, 279−288.

(25) Wiendlocha, B. Resonant Levels, Vacancies, and Doping in Bi_2Te_3, Bi_2Te_2Se, and Bi_2Se_3 Tetradymites. *J. Electron. Mater.* **2016**, *45*, 3515−3531.

(26) Alpichshev, Z.; Biswas, R. R.; Balatsky, A. V.; Analytis, J. G.; Chu, J.-H.; Fisher, I. R.; Kapitulnik, A. STM Imaging of Impurity Resonances on Bi_2Se_3. *Phys. Rev. Lett.* **2012**, *108*, 206402.

(27) Lin, H.; Das, T.; Okada, Y.; Boyer, M. C.; Wise, W. D.; Tomasik, M.; Zhen, B.; Hudson, E. W.; Zhou, W.; Madhavan, V.; et al. Topological Dangling Bonds with Large Spin Splitting and Enhanced Spin Polarization on the Surfaces of Bi_2Se_3. *Nano Lett.* **2013**, *13*, 1915−1919.

(28) Hamers, R. J. Atomic-Resolution Surface Spectroscopy with the Scanning Tunneling Microscope. *Annu. Rev. Phys. Chem.* **1989**, *40*, 531−559.

(29) Kresse, G.; Joubert, D. From Ultrasoft Pseudopotentials to the Projector Augmented-Wave Method. *Phys. Rev. B: Condens. Matter Mater. Phys.* **1999**, *59*, 1758−1775.

(30) Kresse, G.; Furthmüller, J. Efficient Iterative Schemes for Ab Initio Total-Energy Calculations Using a Plane-Wave Basis Set. *Phys. Rev. B: Condens. Matter Mater. Phys.* **1996**, *54*, 11169−11186.

(31) Perdew, J. P.; Burke, K.; Ernzerhof, M. Generalized Gradient Approximation Made Simple. *Phys. Rev. Lett.* **1996**, *77*, 3865−3868.

(32) He, L.; Xiu, F.; Wang, Y.; Fedorov, A. V.; Huang, G.; Kou, X.; Lang, M.; Beyermann, W. P.; Zou, J.; Wang, K. L. Epitaxial Growth of Bi_2Se_3 Topological Insulator Thin Films on Si (111). *J. Appl. Phys.* **2011**, *109*, 103702.

(33) Mann, C.; West, D.; Miotkowski, I.; Chen, Y. P.; Zhang, S.; Shih, C. K. Mapping the 3D Surface Potential in Bi_2Se_3. *Nat. Commun.* **2013**, *4*, 2277.

(34) Zhang, Y.; He, K.; Chang, C.-Z.; Song, C.-L.; Wang, L.-L.; Chen, X.; Jia, J.-F.; Fang, Z.; Dai, X.; Shan, W.-Y.; et al. Crossover of the Three-Dimensional Topological Insulator Bi_2Se_3 to the Two-Dimensional Limit. *Nat. Phys.* **2010**, *6*, 584−588.

(35) Schroder, D. K. *Semiconductor Material and Device Characterization*, 3rd ed.; Wiley-IEEE Press: Hoboken, 2005.

(36) Hikami, S.; Larkin, A. I.; Nagaoka, Y. Spin-Orbit Interaction and Magnetoresistance in the Two Dimensional Random System. *Prog. Theor. Phys.* **1980**, *63*, 707−710.

(37) Bergmann, G. Measurement of the Magnetic Scattering Time by Weak Localization. *Phys. Rev. Lett.* **1982**, *49*, 162−164.

(38) Zhang, M.; Wei, Z.; Jin, R.; Ji, Y.; Yan, Y.; Pu, X.; Yang, X.; Zhao, Y. Electrical Transport Properties and Morphology of Topological Insulator Bi_2Se_3 Thin Films with Different Thickness Prepared by Magnetron Sputtering. *Thin Solid Films* **2016**, *603*, 289−293.

(39) Kim, Y. S.; Brahlek, M.; Bansal, N.; Edrey, E.; Kapilevich, G. A.; Iida, K.; Tanimura, M.; Horibe, Y.; Cheong, S. W.; Oh, S. Thickness-Dependent Bulk Properties and Weak Antilocalization Effect in Topological Insulator Bi_2Se_3. *Phys. Rev. B: Condens. Matter Mater. Phys.* **2011**, *84*, 073109.

(40) Jing, Y.; Huang, S.; Zhang, K.; Wu, J.; Guo, Y.; Peng, H.; Liu, Z.; Xu, H. Q. Weak Antilocalization and Electron-Electron Interaction in Coupled Multiple-Channel Transport in a Bi_2Se_3 Thin Film. *Nanoscale* **2016**, *8*, 1879−1885.

(41) Tkachov, G.; Hankiewicz, E. M. Weak Antilocalization in HgTe Quantum Wells and Topological Surface States: Massive versus Massless Dirac Fermions. *Phys. Rev. B: Condens. Matter Mater. Phys.* **2011**, *84*, 035444.

(42) Vidal, F.; Eddrief, M.; Rache Salles, B.; Vobornik, I.; Velez-Fort, E.; Panaccione, G.; Marangolo, M. Photon Energy Dependence of Circular Dichroism in Angle-Resolved Photoemission Spectroscopy of Bi_2Se_3 Dirac States. *Phys. Rev. B: Condens. Matter Mater. Phys.* **2013**, *88*, 241410.

(43) Sacksteder, V.; Ohtsuki, T.; Kobayashi, K. Modification and Control of Topological Insulator Surface States Using Surface Disorder. *Phys. Rev. Appl.* **2015**, *3*, 064006.